JOURNAL OF MATERIALS RESEARCH AND TECHNOLOGY 2021;15:3598–3609

Available online at www.sciencedirect.com

jmr&t
Journal of Materials Research and Technology

journal homepage: www.elsevier.com/locate/jmrt

Original Article

Effect of microstructure and defect formation on the bending properties of additive manufactured H13 tool steel

Adriel P. Oliveira [a,*], *Luiz H.Q.R. Lima* [b], *Bianca C.A. Felipe* [b], *Claudemiro Bolfarini* [a,b], *Reginaldo T. Coelho* [c], *Piter Gargarella* [a,b,d]

[a] *Graduate Program in Materials Science and Engineering, Federal University of São Carlos, Rod. Washington Luis Km 235, 13565-905, São Carlos, SP, Brazil*

[b] *Department of Materials Engineering (DEMa), Federal University of São Carlos (UFSCar), Rod. Washington Luis Km 235, 13565-905, São Carlos, SP, Brazil*

[c] *Department of Production Engineering, São Carlos Engineering School, University of São Paulo, Av. Trabalhador São-carlense, 400, 13566-590, São Carlos, SP, Brazil*

[d] *Center of Characterization and Development of Materials (CCDM), Federal University of São Carlos (UFSCar), Rod. Washington Luis Km 235, 13565-905, São Carlos, SP, Brazil*

ARTICLE INFO

Article history:
Received 23 August 2021
Accepted 3 October 2021
Available online 8 October 2021

Keywords:
Tool steel
H13
Powder bed fusion
Additive manufacturing
Bending properties

ABSTRACT

Due to its high strength and wear resistance and good fracture toughness at low and high temperatures, AISI H13 tool steel has been widely used to fabricate components such as injection molds, die casting dies, and hot forging tools. Components with complex geometries can be produced by additive manufacturing (AM); however, the success of this manufacture depends on the formed microstructure and mechanical properties, which are associated with the process parameters. The mechanical properties of H13 tool steel processed by AM reported in the literature are limited to those obtained through hardness and tensile tests. Thus, this study aims to correlate the bending properties of H13 tool steel with its microstructure and process parameters when processed by the Powder Bed Fusion (PBF) technique. The samples were produced with different energy densities (approximately 200, 400, and 600 J/mm^3) and analyzed by XRD, OM, SEM, and ACOM-TEM. The amount of retained austenite in the cellular microstructure and the porosity decreased as the energy density increased. The sample manufactured with 400 J/mm^3 presented the highest density and bending stress values. In contrast, the sample produced with 600 J/mm^3 showed a smaller number of defects and more extensive deformation before fracture. This behavior was explained considering the fraction of retained austenite, intrinsic tempering, and presence of defects. The fracture mechanism comprised a mixture of cleavage and dimple formation. This study demonstrates that the bending properties of H13 tool steel processed by PBF are directly related to the resulting microstructure and process parameters used to fabricate the parts.

---

* Corresponding author.
E-mail address: adrielpugliesi@hotmail.com (A.P. Oliveira).

https://doi.org/10.1016/j.jmrt.2021.10.011

1. Introduction

Additive manufacturing (AM) has received considerable attention in recent years because it presents several attractive advantages, such as the possibility to produce parts with design freedom, total automation, sustainability, and cost effectiveness [1]. AM is becoming a reality in medicine, aerospace, and machine tools, with application in rapid prototyping, production of customized items and small batches of very complex components, and repairing products such as molds and dies [2–4].

Powder Bed Fusion (PBF) is the most consolidated AM method to print metallic parts, with more than 50 companies worldwide producing such machines today. Parts are built layer by layer based only on a computer-aided design (CAD) model, using a laser or electron beam as energy source. After printing one layer, the process is repeated, stacking the layers until parts can be 3D-printed with lower roughness and higher accuracy than in other AM methods [1]. Several PBF parameters are important: beam power, scanning speed and strategy, hatching, layer thickness, and powder characteristics [5]. The control of these processing parameters enables manipulation of microstructure, forming out-of-equilibrium phases [6].

Application of AM to produce molds and dies is very promising, because it allows construction of a complex internal cooling system, thus increasing process efficiency and tool life [7,8]. AISI H13 is one of the most used types of steel for these applications because of its high wear resistance and strength and good fracture toughness at low and high temperatures. Several studies have investigated H13 steel obtained by AM [9–19]. Narvan et al. [9] and Bo Ren et al. [10] carried out systematic investigations, and showed that samples with relative density >99% could be obtained using appropriate processing parameters. Many studies have investigated the microstructure and phase formation of as-printed additive manufactured H13 samples [9–15]. A cellular microstructure consisting of martensite and retained austenite is formed, with cell size of approximately 0.5–2 μm. Formation of a very small fraction of nanometer-sized V- and Mo-rich carbides were also observed by Lee et al. [12]. This microstructure gives rise to similar microhardness and tensile strength, but usually with lower elongation values than those of conventionally processed H13 steel (forged and heat-treated) [10,12,16,20].

Heat treatment can considerably improve the strength of H13 steel obtained by AM, as shown by Jujie Yan et al. [13]. Those authors showed that, after tempering at 600 °C, the AM-fabricated H13 steel exhibits ultra-high yield strength around 1483 MPa with ~5.8% ductility. Krell et al. [11] showed that printed samples after tempering at around 550-600 °C exhibited higher strength than samples as-printed and after conventional heat treatment with austenitization followed by tempering. Tempering allows precipitation of secondary carbides in the cellular structure, increasing strength. The conventional treatment (austenitization + tempering) changes the unique cellular microstructure by forming a purely tempered martensite structure of lower strength.

Some studies have shown a propensity of additively manufactured H13 steel for crack formation [9,11]. It is necessary to better understand how these materials fracture to broaden the application of AM to fabricate different H13 steel components for critical structural applications in molds and dies. The strength and toughness of this material, when fabricated by AM, have been almost exclusively investigated in tensile tests [12,13,21,22]. Other tests, such as bending and fracture toughness, should be performed to further understand the potential of AM to produce high-strength components of tool steels.

In this context, the present study aimed to explore the mechanical properties of additively manufactured H13 tool steel samples by submitting them to bending tests. Additionally, a systematic fracture analysis was carried out to investigate how this material fractures. The samples were produced by PBF with optimized parameters and different energy densities. Their microstructure, defective formation, and densification were correlated with their bending behavior and fracture mechanisms.

2. Materials and methods

A commercial gas-atomized AISI H13 steel tool powder manufactured by LPW Technology Ltd. was used to produce the samples in this study. An inductively coupled plasma optical emission spectrometer (VISTA Varian) was used to confirm the chemical composition of the powder, with the carbon element determined by direct combustion in a LECO CS-844 device. Particle size distribution was investigated by sieving, and powder morphology, presence of satellite particles, and microstructure of the different granulometric ranges were analyzed using a Phillips XL-30 FEG scanning electron microscope. For microstructural characterization, the powder was embedded in resin, hand-ground, polished, and then chemically etched Crnkovic solution (100 mL distilled water, 1.2 g picric acid, 1.2 mL HCl, and 10 mL neutral detergent). The phases present in the powder were analyzed in a Bruker XRD 8 Advance X-ray diffractometer (Cu-Kα1) and the peaks were indexed using the Maud software.

The powder was used to produce different samples (15 mm × 15 mm x 5 mm) using Concept Laser M2 Cusing equipment through a Powder Bed Fusion (PBF) process. Based on the density data obtained by pycnometry, three samples with high relative density (>99.5%), produced with different energy densities, were selected for further investigation (more details on the parameter optimization step can be found in the Supplementary Material). The layer thickness set at the machine was 30 μm and the unidirectional chessboard scanning strategy (5 mm squares) without rotation between the layers were used for all samples. The other parameters used for each chosen sample are shown in Table 2.

The samples were cut into two sections: one parallel to the building direction - longitudinal section (L), and other perpendicular to the building direction - transverse section (T). An Olympos BX41M-LED optical microscope (OM) and a Phillips XL-30 FEG scanning electron microscope (SEM) were used in the microstructural characterization. The phases in the samples were investigated using a Simens D5005 X-ray

Diffractometer (Cu-Kα1). Automated crystal orientation and phase mapping in transmission electron microscopy (ACOM-TEM) were carried out using a Astar System Nanomegas coupled to a TEM FEI TECNAI 52-TWIN. The TEM samples were grided to 100 μm and polished using a Gatan precision ionic polishing system, model 691.

Two mechanical characterization techniques were used: Vickers hardness and bending tests. For the Vickers hardness test, a Tech Corp FM-800 Future was used; the applied force was 0.5 kgf with 15 s dwell time. Fifteen indentations were made in different places of the samples to calculate the average hardness value, following the ASTM E92 standard [23]. For the bending test, two specimens were prepared from the longitudinal and transversal sections of each sample, in dimensions of approximately 5 × 3 × 0.5 mm, using a South Bay Technology lapping/polishing fixture, model 150. The thickness of the samples was checked at the four corners and in the center using a micrometer (0.01 mm precision). The variation between measurements was <2% of the measurement average value, as recommended in [24]. The bending tests were performed using Instron 5500 R equipment with a device designed for three-point bending tests, shown in Fig. 1. The deformation rate used was 0.01 mm/min. The fractured samples were analyzed by the aforementioned OM and SEM to understand the fracture mechanisms.

3. Results and discussion

3.1. Powder characterization

Table 1 shows the chemical composition of the H13 powder supplied by the manufacturer (nominal) and the composition experimentally measured. The nominal and measured compositions are very similar, and both are within the values suggested by the ASTM A681 standard [25]. Figure 2 (a) shows the particle size distribution of the powder. It can be observed that the d_{50} is around 25–30 μm and 70% of the powder is < 35 μm. This average size and particle size distribution are similar to those commonly used in PBF of steels [9,10,17,26]. The morphology and presence of satellite particles were observed by SEM, as shown in Fig. 2 (b). The powder morphology is nearly spherical, with a relatively rough surface. A high fraction of satellite particles can be observed. The Supplementary Material contains more images of the powder taken in different size distributions.

Table 1 – Chemical composition of the H13 powder (wt.%) used.

	Fe	C	Mn	Si	Cr	V	W	Mo
Measured	Bal.	0.39	0.44	0.92	5.01	0.92	–	1.34
Nominal	Bal.	0.36	0.4	1.00	5.21	0.90	–	1.47

The x-ray diffraction (XRD) results are shown in Fig. 3. Similar XRD patterns were obtained for the different particle size ranges, with formation of only two phases: martensite and retained austenite. Figure 4 shows the microstructure of the H13 powder, where martensite formed from previous dendrites of austenite coexists with retained austenite, in agreement with the XRD results and the previous literature [27].

3.2. Characterization of printed samples

Three samples with high relative density (>99.5%), produced with different energy densities, were selected for further

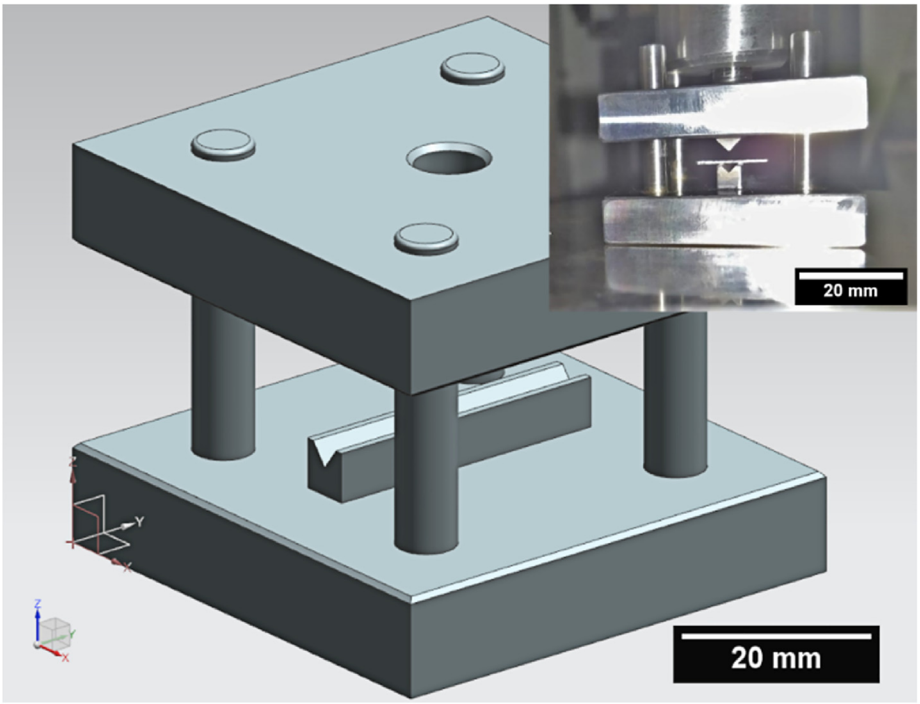

Fig. 1 – Schematic representation of the device used for the three-point bending test. The inset displays the device on the machine with one of the prepared samples.

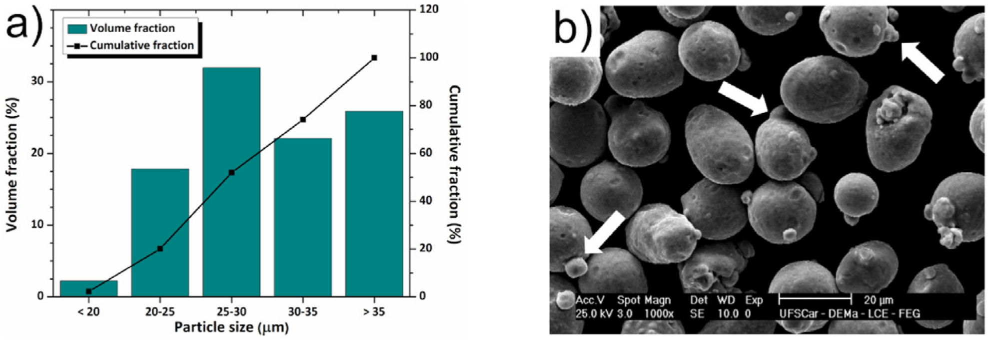

Fig. 2 – a) Particle size distribution of commercial H13 steel powder obtained by gas atomization; b) H13 powder images obtained by SEM for particle size range <20 μm. The white arrows indicate some satellite particles.

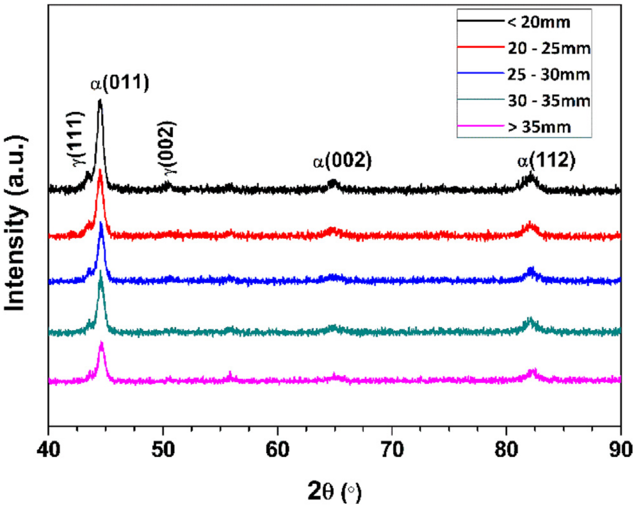

Fig. 3 – Diffractogram of the H13 powder for the different particle size ranges. The small peak located around 56° is an artifact. It does not match any phase present in the sample.

investigation. The parameters used to produce these samples are shown in Table 2, together with the density measured by pycnometry and the relative density based on the theoretical value (7.9 g/cm^3) present in [2]. Although the samples present similar densities, it can be observed that they were produced under completely different energy densities. Their differences in structural and mechanical properties will be discussed ahead in this manuscript.

Figure 5 shows the XRD patterns of the chosen samples taken at the longitudinal and transverse sections. As the powder, the samples present two phases: martensite (a = 2.87 Å, space group: IM-3M) and retained austenite (a = 3.61 Å, space group: FM-3M). According to the quantitative phase analysis performed using the Rietveld method with the Maud software, the volumetric percentage of retained austenite (RA) varied between the samples, and the values are shown in Table 3. As energy density increases, the RA fraction decreases. That is because retained austenite depends on the alloying elements present in solid solution [11,12,15]. With a higher energy input, the layers deposited are reheated for a longer time and with greater intensity. That allows for greater mobility and precipitation of previously trapped elements, which reduces the fraction of retained austenite.

It is also possible to observe that the intensity of the peaks in Fig. 5 changed from one sample section to another, which suggests presence of texture. This is expected in AM samples because of the preferential flow of heat extraction towards the substrate, as previously evidenced in other studies [12,28]. It can also be noted that this variation is more pronounced within the peaks of the austenitic phase. This phenomenon can occur similarly to that observed in maraging steels, where austenite takes on a fibrous texture in the <001> direction.

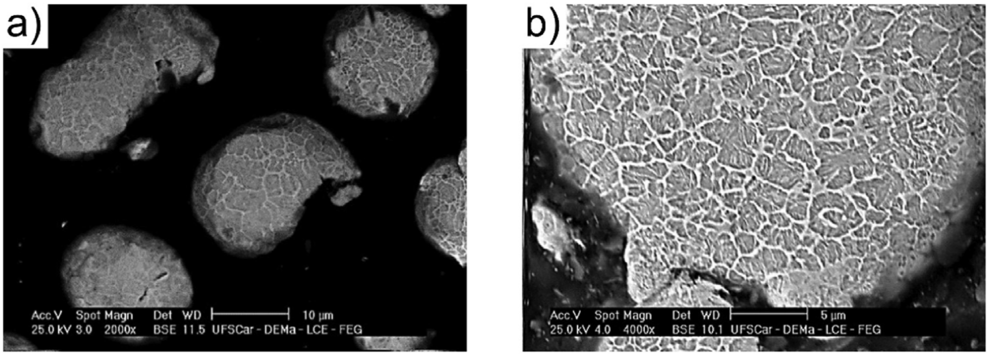

Fig. 4 – SEM micrographs of the H13 powder for the particle size ranges of (a) 20–25 μm and (b)>35 μm.

Table 2 – Samples selected for investigation, named based on their respective approximate energy densities.

Sample	Power (W)	Scanning speed (mm/s)	Hatching (mm)	Layer thickness (mm)	Energy density (J/ mm3)	Pycnometric density (g/cm3)	Relative density (%)
200	350	600	0.090	0.03	216.0	7.892	99.90
400	400	300	0.105	0.03	423.3	7.894	99.92
600	400	200	0.105	0.03	634.9	7.885	99.81

However, martensite is poorly textured, as the martensitic transformation can induce different crystallographic orientations, even starting from an oriented austenite grain, thus minimizing texture effects [15,28].

Figure 6 presents OM images of the top, middle and bottom regions of the three chosen samples on the longitudinal section. For all samples, it is possible to observe the characteristic marks of the different layers deposited. To better quantify the presence of pores, analyses of 15 different images of the longitudinal section of each sample were performed using the ImageJ software. The results are shown in Table 3. Pores decreased with increasing energy density. That happens because a higher energy density increases the depth and width of the molten pool [2]. These factors contribute to reduced lack-of-fusion defects, improving adhesion between layers, and reducing porosity [9,10].

Samples 200 and 400 presented larger fraction of pores than sample 600. This seems contradictory because samples 200 and 400 exhibited slightly higher density than that of sample 600. The volume fraction of the phases may explain this. Austenite presents a higher density than martensite. The larger fraction of retained austenite in samples 200 and 400 (Table 3) might have compensated for the slightly larger fraction of pores in these samples, which may explain the higher density observed.

Additionally, an analysis of the LM observed in the figures was conducted, with five measurements for each image, totaling 15 measurements per sample. These results are also presented in Table 3. It can be observed that the samples with higher energy densities showed greater average spacing between the LM, exceeding the layer thickness value used (30 μm). This indicates that there was greater penetration of the melting pool into the previous layers, which is important to promote a better bonding between layers, avoiding lack-of-fusion defects [2]. Moreover, the sample with the lowest energy density also presented the lowest average spacing between LM and the highest percentage of pores.

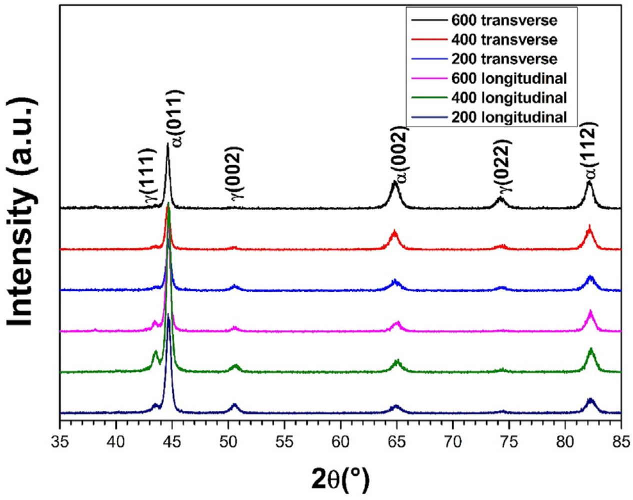

Fig. 5 – X-ray diffraction patterns of the longitudinal and transverse sections of the selected samples.

Table 3 – Values of retained austenite (RA), porosity, and layer marks (LM) found in each of the studied samples.

	200	400	600
RA (%)	18.0 ± 1.1	16.8 ± 1.2	10.1 ± 0.4
Porosity (%)	0.381 ± 0.114	0.365 ± 0.235	0.124 ± 0.010
LM (μm)	30.18 ± 10.61	46.01 ± 9.14	46.46 ± 13.05

Larger spacing, as indicated by the arrows in Fig. 6 (a) and (b), were not included in the mark thickness analysis. According to Deirmina et al. [18], differences in etching contrast indicate regions whose martensite was tempered differently during the intrinsic reheating of the AM process. This may also be the reason why all samples showed a very clear region in the last deposited layers, as seen at the top of the images in Fig. 6 (a), (b), and (c). Therefore, the lighter regions would correspond to less tempered regions, and their appearance, except at the top layers, can be explained by the keyhole melting mode, in which the recoil pressure above the melt pool becomes predominant and exceeds the surface tension of the melted liquid, causing the melt pool to penetrate deep into many previously deposited layers [29,30]. In this case, after solidification, the heat transmitted by the deposition of the next layer may not be sufficient to cause an intrinsic tempering at the bottom of the initial melting pool produced in the keyhole mode, as it will be equivalent to few layers of depth. The largest layer observed in Fig. 6 (b) presented 144.63 μm in its greatest thickness, which would result in a depth of approximately 4.8 layers, considering the thickness of 30 μm used.

The microstructure of sample 400 observed by SEM is shown in Fig. 7. The image was obtained in the central region of the longitudinal section. A cellular structure with martensite cells surrounded by retained austenite was observed for all samples with sizes varying approximately between 0.6 and 2.8 μm. This microstructure is explained by the high cooling rate of the PBF process (around 10^4 K/s) [2,14,27]. Small particles similar to cell walls can be observed within the cell structure. They will be better discussed later. Formation of the cellular microstructure of H13 steel processed by laser-based PBF has been widely reported in the literature [8–10,12,14,15,17,18], and hypotheses about its development can be found in [11]. In this study, all samples

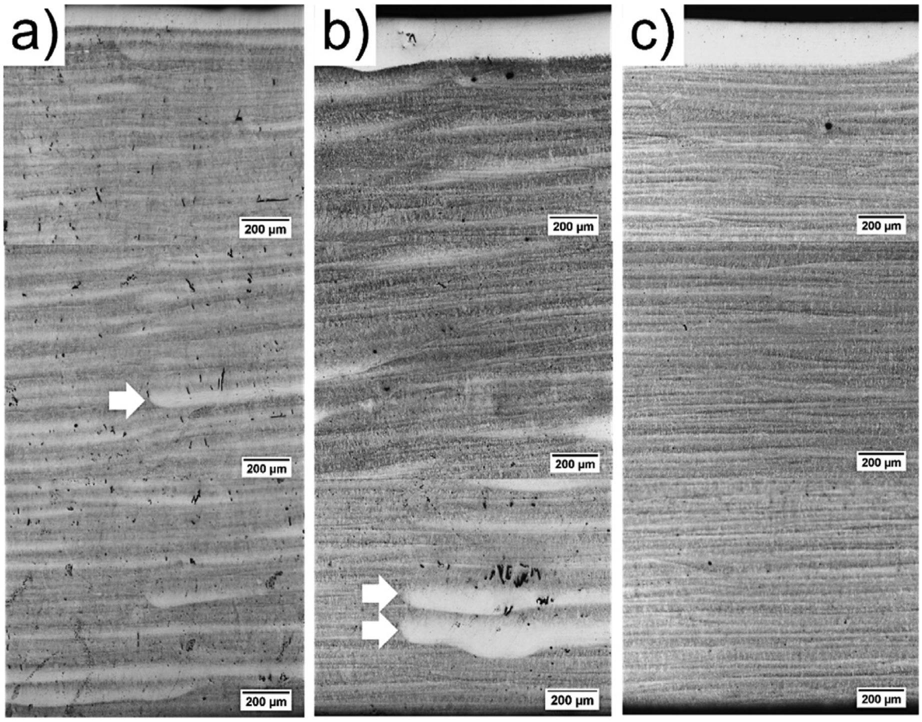

Fig. 6 – Optical micrographs of the longitudinal section of samples 200 (a), 400 (b), and 600 (c) showing top, middle, and bottom regions. The white arrows indicate examples of regions that have been melted in the keyhole mode.

analyzed by SEM presented similar microstructures; images are shown in the Supplementary Material.

Figure 8 shows the TEM images of samples 400 T and 600 T:(a) bright-field image of sample 400- the inset shows a ring diffraction pattern confirming the presence of martensite and retained austenite observed by XRD; (b), (c), and (d) bring the bright-field image of the region analyzed by ACOM-TEM, respectively, the index, reliability, and phase maps (more information about these indices can be found in [31]). Looking at these maps, it is possible to see that the analysis was reliable for almost the entire region, but in some points identified as the retained austenite phase, the indexation was not high. The reason this may be that the region is a phase different from the others, thus it is neither martensite, nor retained austenite (e.g., a precipitate). Another possibility is that the crystalline network in this region is distorted either by residual stresses or elements in a solid solution, hindering indexation.

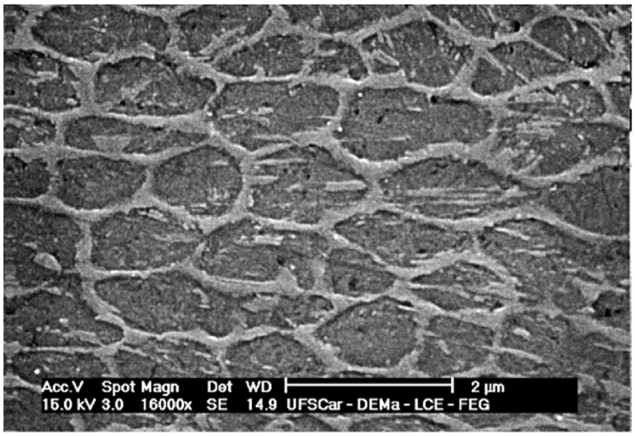

Fig. 7 – SEM micrograph of sample 400. More SEM images of the other selected samples can be found in the Supplementary Material.

In Fig. 8, the images from (f) to (j) follow the same sequential logic as those from (a) to (e), but for the 600 T sample. In the diffraction pattern, only martensite and retained austenite were also identified. The ACOM-TEM analysis showed interesting results for this sample. The reliability of the austenite phases is better compared with that of sample 400. Additionally, it is possible to note that the retained austenite is elongated in some regions, suggesting that the phase present inside the cells shown in Fig. 7 can also be retained austenite between the martensite laths. More studies need to be conducted to clarify this effect and how retained austenite can also form inside cells.

3.3. *Mechanical properties*

Table 4 shows the Vickers hardness values found for each sample in the two sections analyzed. Considering the standard deviation, no significant difference in Vickers hardness is observed between sections of the same sample. Sample 600 showed lower Vickers hardness as a result of the higher energy density, which imposes an elevated heat flow towards the substrate, favoring intrinsic tempering [2,18,32]. This effect causes a natural heat treatment during the process that

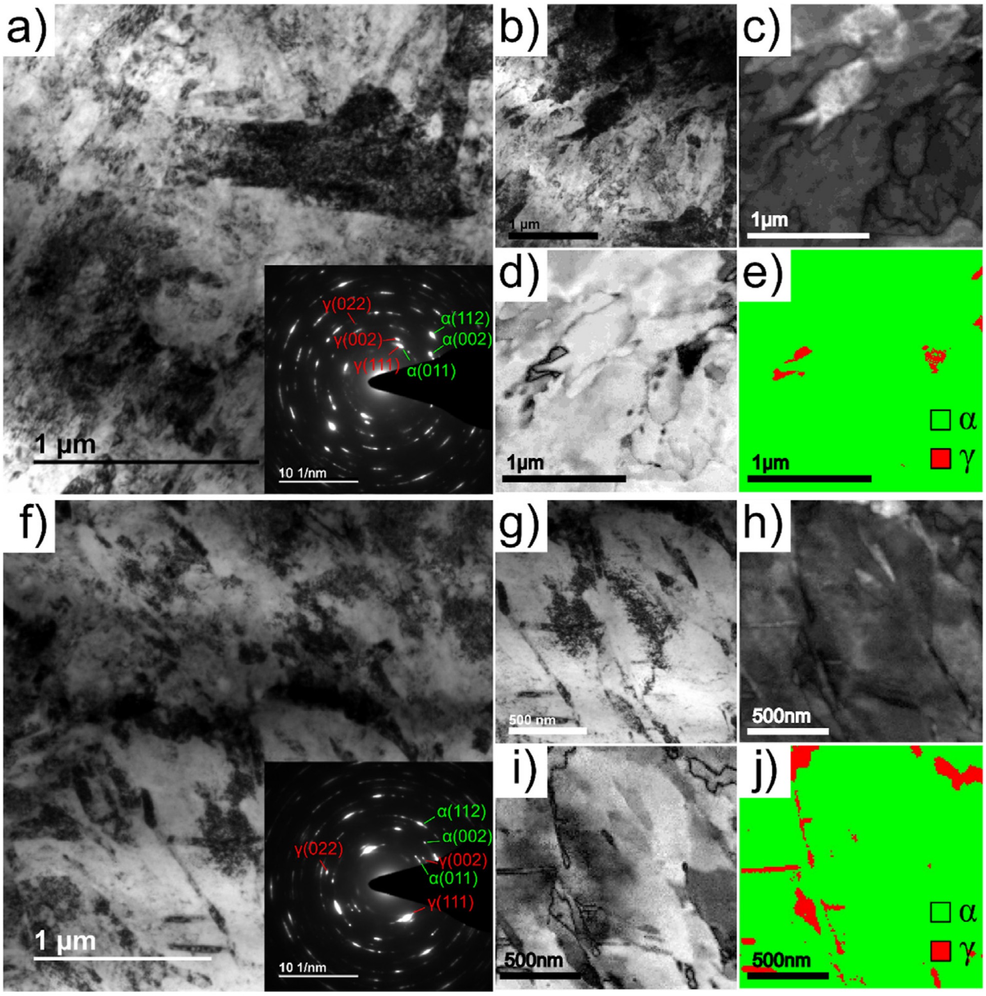

Fig. 8 – (a) TEM bright-field image of sample 400 T. The inset shows the electron diffraction pattern. (b) TEM bright-field image of the region analyzed by ACOM-TEM. (c) Index, (d) reliability, and (e) phase maps built by ACOM-TEM. The images from (f) to (j) show the same sequence as those from (a) to (e), but for the 600 T sample.

can favor annihilation of the dislocations, tempering of the supersaturated martensite, and relief of the residual stresses resulting from the rapid solidification of the layers, thus reducing the Vickers hardness of the sample.

Figure 9 shows the Flexure stress *vs.* flexure extension curves measured for four different specimens of each sample, with two of them taken transversely and two longitudinally. The bending stress was calculated from the following equation: $\sigma_F = (1.5FL)/(bt^2)$, where: F is the applied load, L is the distance between the two points, and b and t are the width and thickness of the specimens, respectively.

Sample 200 showed the lowest bending stress maximum values, as well as relatively little plastic deformation, which is

Table 4 – Vickers hardness test results for the samples in two distinct sections (HV 0.5).

200 L	200 T	400 L	400 T	600 L	600 T
644 ± 11	653 ± 16	657 ± 11	658 ± 21	601 ± 29	643 ± 14

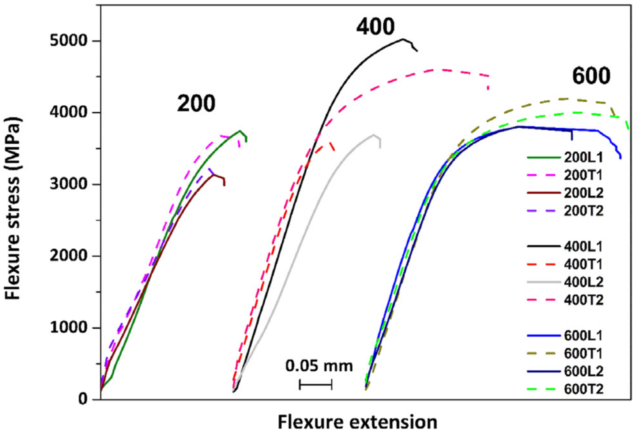

Fig. 9 – Bending test results for the different samples. L and T indicate the direction (longitudinal or transverse, respectively) parallel to the largest surface of the specimen. The numbers 1 and 2 are just to differentiate the specimens produce for the same sample.

accounted for the large number of defects in that sample. One of the specimens from sample 400 showed the highest flexural stress recorded among all, while the other presented performance similar to that of sample 200. Sample 400 showed the most significant difference between the two tested specimens. This can be explained by the intermediate number of defects present, which are often not evenly distributed, as can be observed at the bottom of Fig. 6 (b). That may have contributed to weakening the material. Probably, the region from which the second specimen of sample 400 was taken had more defects and was determining of its poor performance. Sample 600 showed intermediate flexural stress values, but the highest extension values. Furthermore, the maximum stress values were higher for the transverse section. This may be the effect of the texture observed previously. Because this effect was subtle, it was more noticeable in this sample due to its smaller number of defects.

Figure 10 shows the cracks formed during the bending tests. Images 10 (a), (b), and (c) were obtained by OM and show, in addition to the cracks, the marks of the tracks deposited (dotted lines) during the PBF of samples 200T1, 400L1, and 600L2, respectively. It is possible to observe that the cracks started in regions that do not coincide with their edges or the melting pool boundary. It can also be noted that the cracks in images 10(a) and (b) show more abrupt changes in direction than that in image 10(c), which may be associated with the larger number of defects in these samples, which can also be perceived by their worse performances, shown in Fig. 9.

Images 10 (d) and (e) are from samples 600T2 and 600L2, respectively, and were obtained by SEM to observe the path taken by the crack in the microstructure. It is not possible to specify, in these images, any preference for the propagation path in the cellular microstructure. These results demonstrate that defects such as pores and cracks formed during processing have greater influence on mechanical failure and crack path than phase formation and cellular structure.

Figure 11 shows the fracture surfaces of samples 200 L, 400 L, and 600 L. In image (b), the presence of lamellae on the fracture surface stands out. Sample 200 was the only one that showed this characteristic, which is believed to be associated with a large number of microcracks present in this sample. To better explain this characteristic, one can look at Fig. 12, which is also from sample 200, but from another region examined in preliminary analyses. Some microcracks (of few microns in size) are present in the contours of the cellular microstructure. Figure 12 (a) shows the transverse section, while Fig. 12 (b) shows the longitudinal section, where it can be observed that the microcrack, in addition to being located around the cell structure, separates two regions with different growth directions. The origin of such microcracks can be the result of residual stresses caused by the high-temperature gradient imposed by the laser. In this case, the heat-affected zone expands with increasing temperature, but its expansion is limited by the lower layers or the substrate, thus generating compression stresses. In contrast, when the molten pool solidifies and cools quickly, the surface layer tends to contract and, again, is prevented by the lower layers, which generates tensile stresses. If the stress exceeds the material ultimate tensile strength, cracks can occur [2,33].

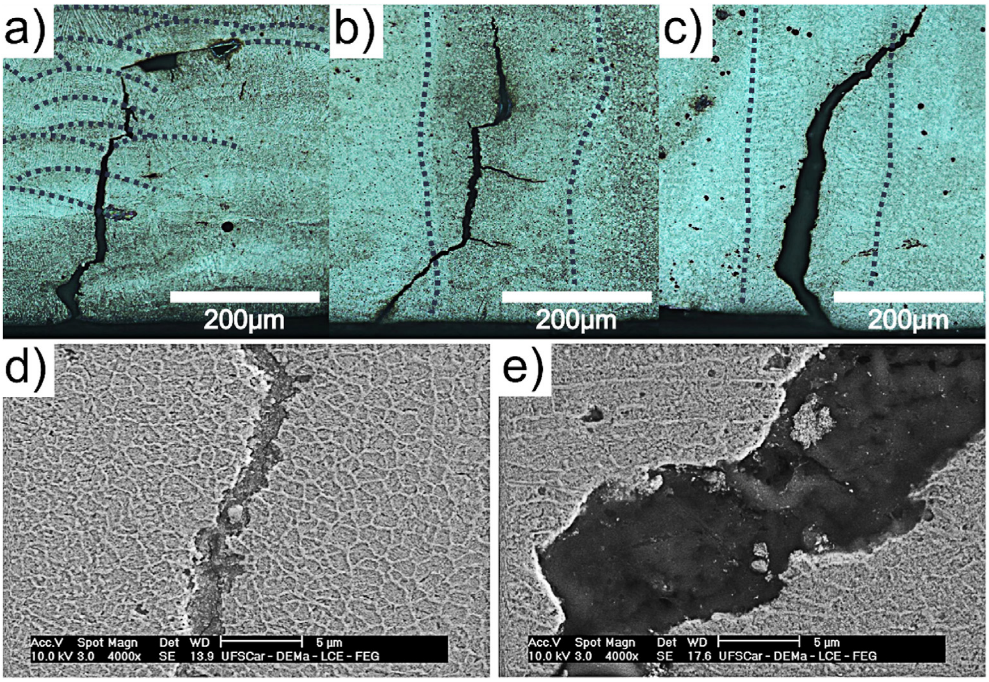

Fig. 10 – Images of the cracks formed in the fractured bending test samples: a), b), and c), are OM images of the fractured 200 T1, 400 L1, and 600L2 samples, respectively (some track outlines have been highlighted for easy viewing.); d) and e) are SEM images of the fractured 600T2 and 600L2 samples, respectively.

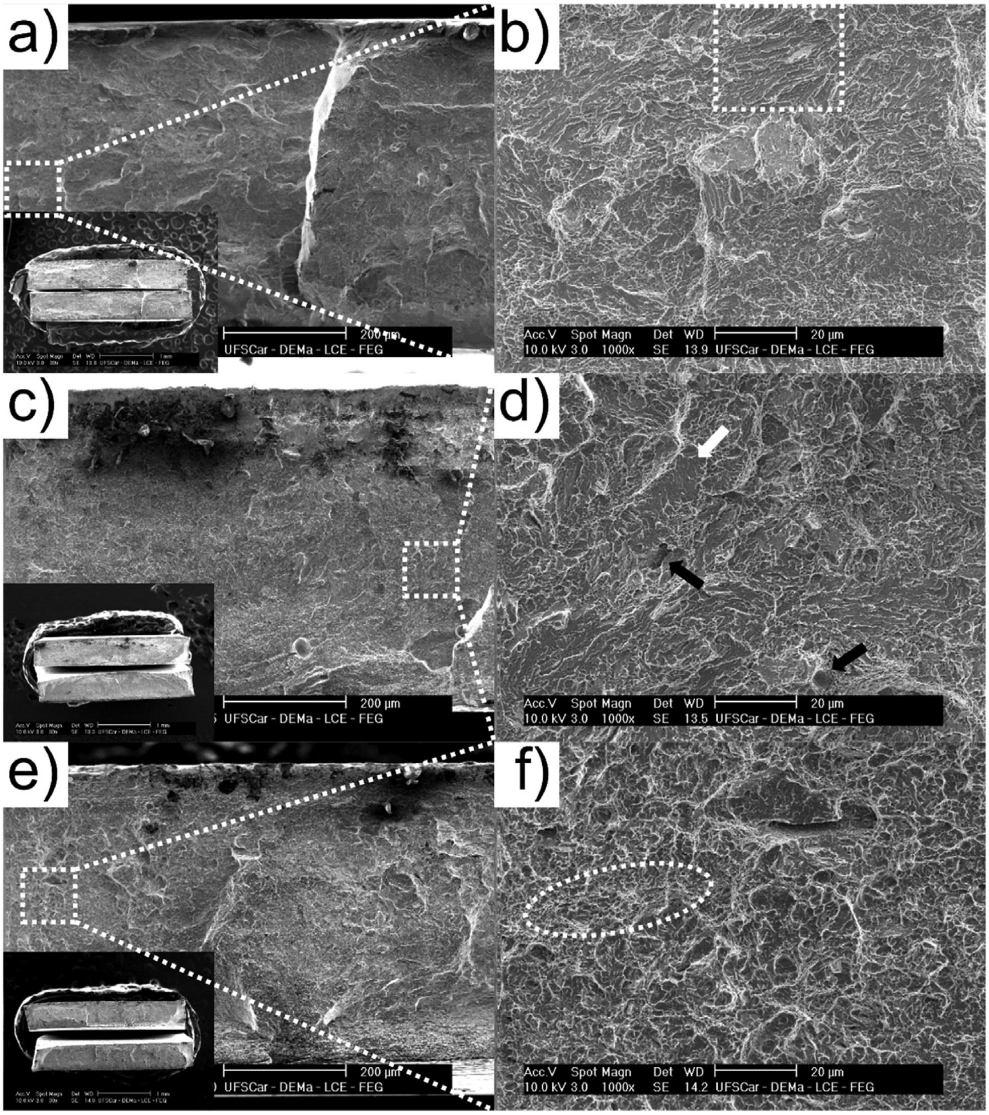

Fig. 11 – SEM images of fracture surfaces with different magnifications: a) and b) sample 200L2 - the rectangle indicates the presence of lamellae; c) and d) sample 400L2 - the white arrow indicates cleavage marks and the black arrows point to defects (crack and pore); e) and f) sample 600L1 - the circle highlights small dimples.

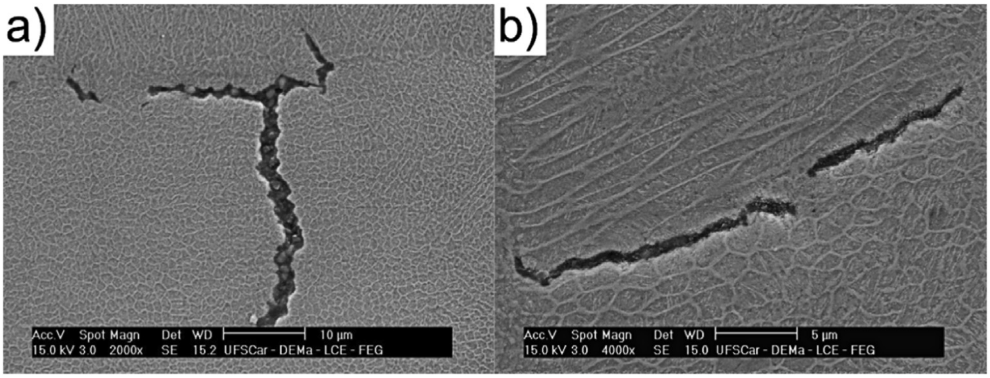

Fig. 12 – Examples of microcracks present in sample 200 T: a) transverse section; b) longitudinal section.

However, the cracks in Fig. 12 are also somewhat similar to the solidification cracks often observed in nickel superalloys, or even in high-entropy alloys processed by AM [34,35]. The solidification cracks appear in the final stages of solidification, when the thermal contraction of the already solidified fraction causes tensions that the liquid fraction is not able to withstand, generating cracks. This problem is more commonly found in alloys that present high thermal expansion coefficients and large solidification intervals. Solute segregation is another risk factor, as it can locally lower the melting point [2,36]. Lee et al. [12] and Fonseca et al. [15] have demonstrated that there is solute segregation at the edges of the H13 steel cellular microstructure processed by PBF, which is also considered to be one of the causes of retained austenite formation. Krell et al. [11] observed through thermodynamic simulations using the Scheil model that the H13 solidification interval is more expressive due to solute segregation. Based on this information, we believe that the cracks observed in sample 200 could be solidification microcracks.

In welding, it is known that presence of solidification cracks can show a dendritic morphology on the fracture surface [36]. Guo et al. [34] observed dendritic morphology on fractured surfaces by tensile tests on high-entropy FeCoCrNiMn-(N, Si) alloys processed by PBF, and associated these findings with solidification cracks. Dörfert et al. [19] found lamellar structures on the fracture surface of H13 steel samples tested for fatigue, without attributing such lamellae to any fatigue fracture mechanism or addressing possible causes. Similar structures were also identified in the fractures of H13 steel processed by PBF by Džugan et al. [21] after tensile tests. Figure 13 suggests a schematic representation to explain how the lamellar structure can be seen on the fracture surface as a result of presence of solidification microcracks. Images 13 (a) and (b) define an imaginary volume in the material where a

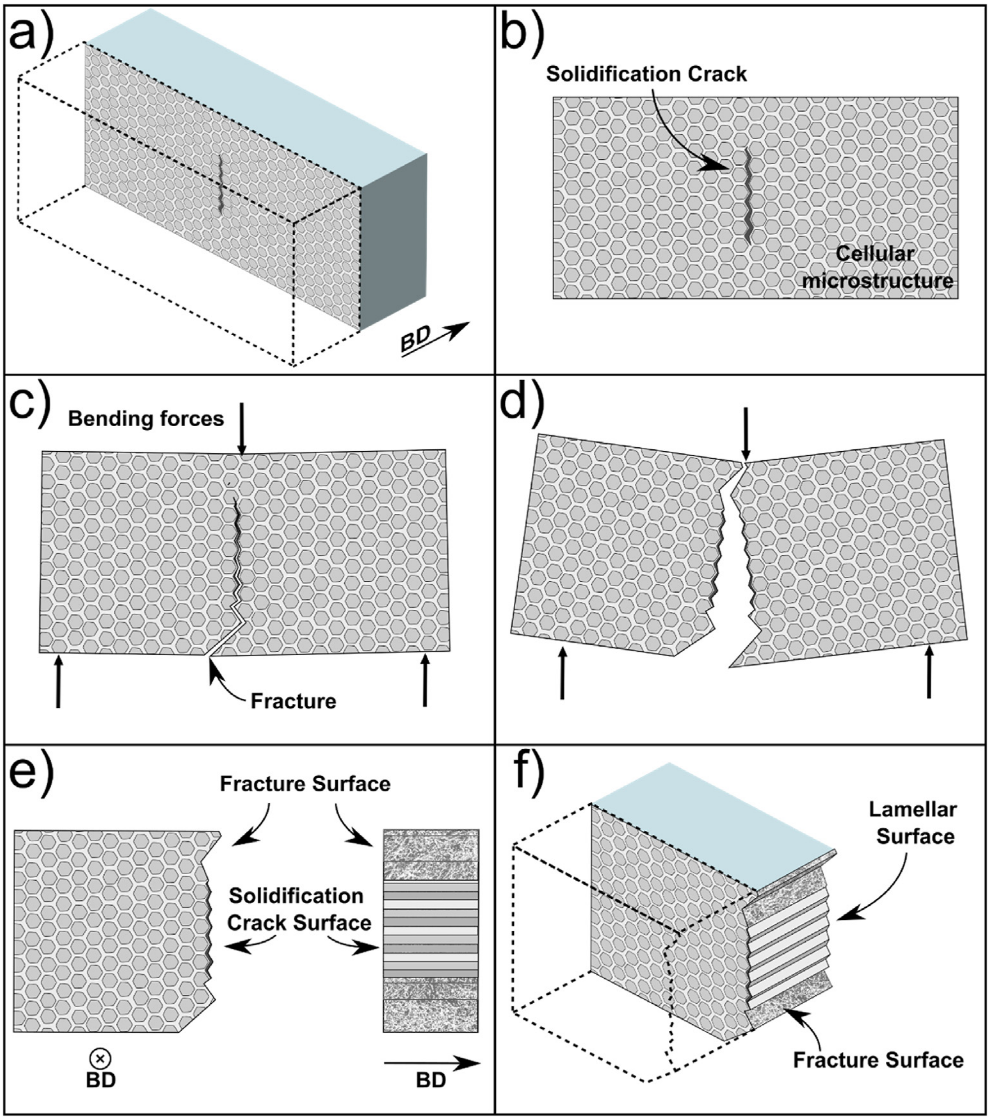

Fig. 13 – Schematic representation of the lamellar structure formation observed on the fracture surface: a) and b) show an imaginary volume with a microcrack in the contour of the cellular microstructure; c) and d) show the fracture during the bending test, taking advantage of the existence of the microcrack; e) and f) show a representation of the fracture surface with the lamellae.

solidification microcrack exists in the contour of the cellular microstructure. Images 13 (c) and (d) show how the fracture can originate or take advantage of preexisting microcracks to minimize the energy required for propagation. Finally, images 13 (e) and (f) show the emergence of lamellae on the fracture surface. It is interesting to note that the presence of microcracks in cellular morphology can lead to the observation of lamellae on the fracture surface in different types of mechanical tests other than the bending test.

Referring back to Fig. 11, samples 400 L and 600 L are also displayed in images d) and f), respectively. The black arrows indicate the existence of some micro defects, such as cracks and pores, whereas the white arrow indicates one of the places where cleavage failure is evident. It can be observed that the fracture mechanism was mainly cleavage with formation of some dimples (quasi-cleavage) in sample 600. This is in line with previous literature reports. Ren et al. [10] noted that tensile stresses cause a quasi-cleavage fracture in as-printed H13 steel samples processed by PBF. They claimed that the presence of retained austenite, which presents a more ductile phase than martensite, favored the formation of dimples. Yan et al. [13] observed only cleavage in their as-printed H13 steel samples, but formation of dimples occurred after tempering heat treatments at 600 °C. Other authors have also observed fracture resulting from quasi-cleavage after stress relief treatments in printed H13 steel samples [21,22]. In conclusion, the high resistance of H13 steel together with some defects imposed by the AM process makes this material present a predominantly fragile fracture, as observed in this study in samples 200 and 400. However, the small number of defects present in sample 600, combined with the high energy density imposed during the process and the consequent intrinsic tempering undergone by this sample, contribute to the quasi-cleavage fracture mechanism presented by this sample, in agreement with its greater extension observed during the bending tests.

4. Conclusions

- Cellular structure with sizes varying approximately between 0.6 and 2.8 μm containing martensite cells surrounded by retained austenite was observed for all samples. It was observed that the amount of retained austenite and porosity decreases with increasing the energy density applied.
- The densest sample was conceived with an energy density of 423.3 J/mm^3, presenting the highest bending stress values; however, sample 600 (634,9 J/mm^3) presented the smallest number of defects and greater fracture extension. Therefore, the relative density is not inversely proportional to the number of defects. The retained austenite fraction, which is a phase denser than martensite, may explain this apparent contradiction.
- Fracture is ruled by the defects formed during processing, such as microcracks and porosity, without a significant effect of phase formation or cell dimensions, and its mechanism involves mainly cleavage with some dimple formation, observed in sample 600.
- Some regions of the fracture surface of sample 200 showed a lamellar structure, which is believed to be the interior of the solidification microcracks observed in the failure plane.
- The bending test was shown to be more sensitive to part defects than the Vickers hardness test, being an interesting alternative to evaluate the mechanical performance of small samples. This can assist in obtaining optimum parameters for parts produced by AM.

Declaration of Competing Interest

The authors declare that they have no known competing financial interests or personal relationships that could have appeared to influence the work reported in this paper.

Acknowledgments

This study was financed in part by the Coordenação de Aperfeiçoamento de Pessoal de Nível Superior—Brazil (CAPES) - Finance Code 001. The authors would like to thank the São Paulo Research Foundation (FAPESP) for the financial support received through project nos. 2016/11309-0, 2017/27031-4, and 2018/15659-1. The authors are also grateful to the Instituto SENAI de Inovação em Laser for the support with preparation of the PBF samples.

Appendix A. Supplementary data

Supplementary data to this article can be found online at https://doi.org/10.1016/j.jmrt.2021.10.011.

REFERENCES

[1] Herzog D, Seyda V, Wycisk E, Emmelmann C. Acta materialia additive manufacturing of metals. Acta Mater 2016;117:371–92. https://doi.org/10.1016/j.actamat.2016.07.019.

[2] DebRoy T, Wei HL, Zuback JS, Mukherjee T, Elmer JW, Jo Milewski, et al. Additive manufacturing of metallic components – process, structure and properties. Prog Mater Sci 2018;92:112–224. https://doi.org/10.1016/j.pmatsci.2017.10.001.

[3] Jhavar S, Paul CP, Jain NK. Causes of failure and repairing options for dies and molds: a review. Eng Fail Anal 2013;34:519–35. https://doi.org/10.1016/j.engfailanal.2013.09.006.

[4] Batalha RL, Batalha WC, Deng L, Gustmann T, Pauly S, Kiminami CS, et al. Processing a biocompatible Ti-35Nb-7Zr-5Ta alloy by selective laser melting. J Mater Res 2020;35:1143–53. https://doi.org/10.1557/jmr.2020.90.

[5] Gustmann T, Dos Santos JM, Gargarella P, Kühn U, Van Humbeeck J, Pauly S. Properties of Cu-based shape-memory alloys prepared by selective laser melting. Shape Mem Superelas 2017;3:24–36. https://doi.org/10.1007/s40830-016-0088-6.

[6] Pollock TM, Clarke AJ, Babu SS. Design and tailoring of alloys for additive manufacturing. Metall Mater Trans A Phys Metall Mater Sci 2020;51:6000–19. https://doi.org/10.1007/s11661-020-06009-3.

[7] Mazur M, Leary M, McMillan M, Elambasseril J, Brandt M. SLM additive manufacture of H13 tool steel with conformal cooling and structural lattices. Rapid Prototyp J 2016;22:504–18. https://doi.org/10.1108/RPJ-06-2014-0075.

[8] Wang J. A short review on selective laser melting of H13 steel. 2020. p. 2453–66.

[9] Narvan M, Al-Rubaie KS, Elbestawi M. Process-structure-property relationships of AISI H13 tool steel processed with selective laser melting. Materials 2019;12:1–20. https://doi.org/10.3390/ma12142284.

[10] Ren B, Lu D, Zhou R, Li Z, Guan J. Preparation and mechanical properties of selective laser melted H13 steel. J Mater Res 2019;34:1415–25. https://doi.org/10.1557/jmr.2019.10.

[11] Krell J, Röttger A, Geenen K, Theisen W. General investigations on processing tool steel X40CrMoV5-1 with selective laser melting. J Mater Process Technol 2018;255:679–88. https://doi.org/10.1016/j.jmatprotec.2018.01.012.

[12] Lee J, Choe J, Park J, Yu JH, Kim S, Jung ID, et al. Microstructural effects on the tensile and fracture behavior of selective laser melted H13 tool steel under varying conditions. Mater Char 2019;155:109817. https://doi.org/10.1016/j.matchar.2019.109817.

[13] Yan J, Song H, Dong Y, Quach WM, Yan M. High strength (~2000 MPa) or highly ductile (~11%) additively manufactured H13 by tempering at different conditions. Mater Sci Eng A 2020;773:138845. https://doi.org/10.1016/j.msea.2019.138845.

[14] Yan JJ, Zheng DL, Li HX, Jia X, Sun JF, Li YL, et al. Selective laser melting of H13: microstructure and residual stress. J Mater Sci 2017;52:12476–85. https://doi.org/10.1007/s10853-017-1380-3.

[15] Fonseca EB, Gabriel AHG, Araújo LC, Santos PLL, Campo KN, Lopes ESN. Assessment of laser power and scan speed in fl uence on microstructural features and consolidation of AISI H13 tool steel processed by additive manufacturing. Addit Manuf 2020;34:101250. https://doi.org/10.1016/j.addma.2020.101250.

[16] Mertens R, Vrancken B, Holmstock N, Kinds Y, Kruth J-P, Van Humbeeck J. Influence of powder bed preheating on microstructure and mechanical properties of H13 tool steel SLM parts. Phys Procedia 2016;83:882–90. https://doi.org/10.1016/J.PHPRO.2016.08.092.

[17] Wang M, Li W, Wu Y, Li S, Cai C, Wen S, et al. High-temperature properties and microstructural stability of the AISI H13 hot-work tool steel processed by selective laser melting. Metall Mater Trans B Process Metall Mater Process Sci 2019;50:531–42. https://doi.org/10.1007/s11663-018-1442-1.

[18] Deirmina F, Peghini N, AlMangour B, Grzesiak D, Pellizzari M. Heat treatment and properties of a hot work tool steel fabricated by additive manufacturing. Mater Sci Eng A 2019;753:109–21. https://doi.org/10.1016/j.msea.2019.03.027.

[19] Dörfert R, Zhang J, Clausen B, Freiße H, Schumacher J, Vollertsen F. Comparison of the fatigue strength between additively and conventionally fabricated tool steel 1.2344. Addit Manuf 2019;27:217–23. https://doi.org/10.1016/j.addma.2019.01.010.

[20] Mazur M, Brincat P, Leary M, Brandt M. Numerical and experimental evaluation of a conformally cooled H13 steel injection mould manufactured with selective laser melting. Int J Adv Manuf Technol 2017;93:881–900. https://doi.org/10.1007/s00170-017-0426-7.

[21] Džugan J, Halmešová K, Ackermann M, Koukolíková M, Trojanová Z. Thermo-physical properties investigation in relation to deposition orientation for SLM deposited H13 steel. Thermochim Acta 2020;683:178479. https://doi.org/10.1016/j.tca.2019.178479.

[22] Åsberg M, Fredriksson G, Hatami S, Fredriksson W, Krakhmalev P. Influence of post treatment on microstructure, porosity and mechanical properties of additive manufactured H13 tool steel. Mater Sci Eng A 2019;742:584–9. https://doi.org/10.1016/j.msea.2018.08.046.

[23] ASTM92-17. Standard test methods for Vickers hardness and knoop hardness of metallic materials. West Conshohocken, PA: ASTM International; 2017. p. 1–27. https://doi.org/10.1520/E0092-17.2.

[24] ASTM E. 855-90: standard test methods for bend testing of metallic flat materials for spring applications involving static loadingvol. 1; 2000. p. 1–8. https://doi.org/10.1520/E0855-08R13.2. 90.

[25] Specification S. Standard Specification for Tool Steels Alloy. 1; 2005. p. 1–14. https://doi.org/10.1520/A0681-08.2. 94.

[26] Ackermann M, Šafka J, Voleský L, Bobek J, Kondapally JR. Impact testing of H13 tool steel processed with use of selective laser melting technology. Mater Sci Forum 2018;919:43–51. https://doi.org/10.4028/www.scientific.net/MSF.919.43.

[27] Yan J, Zhou Y, Gu R, Zhang X, Quach WM, Yan M. A comprehensive study of steel powders (316L, H13, P20 and 18Ni300) for their selective laser melting additive manufacturing. Metals 2019;9. https://doi.org/10.3390/met9010086.

[28] Bajaj P, Hariharan A, Kini A, Kürnsteiner P, Raabe D, Jägle EA. Steels in additive manufacturing: a review of their microstructure and properties. Mater Sci Eng A 2019;772:138633. https://doi.org/10.1016/J.MSEA.2019.138633.

[29] de Terris T, Andreau O, Peyre P, Adamski F, Koutiri I, Gorny C, et al. Optimization and comparison of porosity rate measurement methods of Selective Laser Melted metallic parts. Addit Manuf 2019;28:802–13. https://doi.org/10.1016/j.addma.2019.05.035.

[30] Khairallah SA, Anderson AT, Rubenchik A, King WE. Laser powder-bed fusion additive manufacturing: physics of complex melt flow and formation mechanisms of pores, spatter, and denudation zones. Acta Mater 2016;108:36–45. https://doi.org/10.1016/j.actamat.2016.02.014.

[31] Rauch EF, Véron M. Automated crystal orientation and phase mapping in TEM. Mater Char 2014;98:1–9. https://doi.org/10.1016/j.matchar.2014.08.010.

[32] Zuback JS, DebRoy T. The hardness of additively manufactured alloys. Materials 2018;11. https://doi.org/10.3390/ma11112070.

[33] He Y, Zhong M, Beuth J, Webler B. A study of microstructure and cracking behavior of H13 tool steel produced by laser powder bed fusion using single-tracks, multi-track pads, and 3D cubes. J Mater Process Technol 2020;286:116802. https://doi.org/10.1016/j.jmatprotec.2020.116802.

[34] Guo L, Gu J, Gan B, Ni S, Bi Z, Wang Z, et al. Effects of elemental segregation and scanning strategy on the mechanical properties and hot cracking of a selective laser melted FeCoCrNiMn-(N,Si) high entropy alloy. J Alloys Compd 2021:865. https://doi.org/10.1016/j.jallcom.2021.158892.

[35] Nie P, Ojo OA, Li Z. Numerical modeling of microstructure evolution during laser additive manufacturing of a nickel-based superalloy. Acta Mater 2014;77:85–95. https://doi.org/10.1016/j.actamat.2014.05.039.

[36] Kou S. Solidification and liquation cracking issues in welding. JOM (J Occup Med) 2003;55:37–42. https://doi.org/10.1007/s11837-003-0137-4.